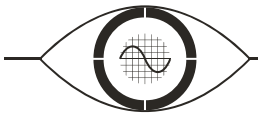

Lehrstuhl für Bildverarbeitung
Institute of Imaging & Computer Vision

A Two-Stage Approach for Fully Automatic Segmentation of Venous Vascular Structures in Liver CT Images

Jens N. Kaftan and Hüseyin Tek and Til Aach

Institute of Imaging and Computer Vision
RWTH Aachen University, 52056 Aachen, Germany
tel: +49 241 80 27860, fax: +49 241 80 22200
web: www.lfb.rwth-aachen.de

in: Medical Imaging 2009: Image Processing. See also BibTeX entry below.

BibTeX:

```
@inproceedings{KAF09a,
author    = {Jens N. Kaftan and H{\" u}seyin Tek and Til Aach},
title     = {A Two-Stage Approach for Fully Automatic Segmentation of Venous Vascular Structures in Liver {CT} Imag
booktitle = {Medical Imaging 2009: Image Processing},
editor    = {J. P. W. Pluim and B. M. Dawant},
publisher = {SPIE},
volume    = {7259},
address   = {Orlando, USA},
month     = {February 7--12},
year      = {2009},
pages     = {725911-1--12}}
```


document created on: July 10, 2009
created from file: livervesselsegmentation.tex
cover page automatically created with CoverPage.sty
(available at your favourite CTAN mirror)

RWTH AACHEN
RHEINISCH-WESTFÄLISCHE TECHNISCHE HOCHSCHULE AACHEN

A Two-Stage Approach for Fully Automatic Segmentation of Venous Vascular Structures in Liver CT Images

Jens N. Kaftan[ab], Hüseyin Tek[c], and Til Aach[a]

[a]Institute of Imaging and Computer Vision, RWTH Aachen University,
Templergraben 55, 52056 Aachen, Germany
[b]Siemens Healthcare Sector, Computed Tomography,
Siemensstr. 1, 91301 Forchheim, Germany
[c]Siemens Corporate Research, 755 College Road East, Princeton, NJ 08540, USA

ABSTRACT

The segmentation of the hepatic vascular tree in computed tomography (CT) images is important for many applications such as surgical planning of oncological resections and living liver donations. In surgical planning, vessel segmentation is often used as basis to support the surgeon in the decision about the location of the cut to be performed and the extent of the liver to be removed, respectively. We present a novel approach to hepatic vessel segmentation that can be divided into two stages. First, we detect and delineate the core vessel components efficiently with a high specificity. Second, smaller vessel branches are segmented by a robust vessel tracking technique based on a medialness filter response, which starts from the terminal points of the previously segmented vessels. Specifically, in the first phase major vessels are segmented using the globally optimal graph-cuts algorithm in combination with foreground and background seed detection, while the computationally more demanding tracking approach needs to be applied only locally in areas of smaller vessels within the second stage. The method has been evaluated on contrast-enhanced liver CT scans from clinical routine showing promising results. In addition to the fully-automatic instance of this method, the vessel tracking technique can also be used to easily add missing branches/sub-trees to an already existing segmentation result by adding single seed-points.

Keywords: segmentation, hepatic vessel, liver, computed tomography

1. INTRODUCTION

The accurate and robust detection and delineation of vascular structures within the liver is an important prerequisite for different medical applications. Especially for surgical planning, the knowledge of the individual 3D vessel tree structures is extremely helpful to analyze affected vessels and liver regions that will be disconnected from blood supply after the operation. For example, the required extent of oncologic resections is dependent on the location of the tumor in relation to the major vessels that define the liver's surgical anatomy. Even more important are 3D planning techniques in the field of minimally invasive surgery, which generally permits less complete visualization during the procedure [1]. Also radio frequency (RF) ablation treatments require planning for which the spatial relationship of a lesion with respect to major vessels and branches needs to be visualized and analyzed. Such planning tools may also be helpful in biopsy path planning. Additionally, for living donor liver transplantation [2, 3] the branching pattern of the vessel systems needs to be analyzed to support the decision regarding the suitability of the donor. In particular the determination of liver volume is important to ensure adequate postoperative liver function for donor and recipient. Finally, the commonly accepted Couinaud's partitioning scheme [4] is defined by the main portal and hepatic vein branches.

The segmentation of vascular structures in contrast-enhanced liver CT images is challenging because of the high variability of the liver and vascular anatomy and the typically low constrast between vessels and the surrounding liver tissue. Also the distribution of the contrast-agent depends on the bolus phase resulting in an varying amount of contrast in the image as well as in varying enhancement within the vacular trees. Additionally,

Further author information: (Send correspondence to J. N. Kaftan)
E-mail: jens.kaftan@lfb.rwth-aachen.de, Telephone: +49 241 80 27974

Medical Imaging 2009: Image Processing, edited by Josien P. W. Pluim, Benoit M. Dawant,
Proc. of SPIE Vol. 7259, 725911 · © 2009 SPIE
CCC code: 1605-7422/09/$18 · doi: 10.1117/12.812407

bright non-vascular structures such as contrast-enhanced tumors might cause leakages in intensity-based vessel segmentation algorithms.

Typical segmentation approaches often include noise reduction and background compensation [5] or vessel-enhancement methods [6,7] as pre-processing steps followed by variations of region growing techniques [5–7] and further post-processing steps such as centerline extraction and tree separation algorithms. A review on vessel segmentation methods with application to hepatic vessel segmentation can be also found in [8].

Soler *et al.* [9,10] use anisotropic diffusion as pre-processing step to reduce the noise inside the liver mask while preserving structural borders. An initial segmentation is obtained by dividing the set of voxels into three classes representing lesions, parenchyma, and vessels via thresholding. The thresholds are estimated based on the intensity histogram. Subsequently, the vessel segmentation is refined by first adding voxels from the parenchyma class to the vessel class that are brighter than a certain threshold within a morphological closing step and then removing false branches based on geometrical and topological properties of the resulting skeleton structure.

Selle *et al.* [5,11,12] use different filters (Gaussian, median, Laplace-like) to remove noise and to compensate for intensity variations within the liver parenchyma. Starting from an interactively selected seed-point, an intensity-based region growing is applied with decreasing thresholds, while the optimal threshold is determined based on the number of segmented voxels at each threshold.

Other approaches use the response of a multi-scale vessel enhancement filter as basis for segmentation. For example, Beichel *et al.* [7] use the Hessian-based filter as defined in [13] while Erdt *et al.* [6] use a novel combination of the resulting eigenvalues of the Hessian matrix that maximizes the filter response for ideal tubular structures without any further parameters than the scale factor. Additionally they have shown, that such a filter can be efficiently computed utilizing the GPU.

Recently, two independent approaches that are partly related to the different stages of our work have been proposed. First, a semi-automatic graph-based method [14] has been applied that uses graph-cuts to segment venous hepatic structures. To this end, the user is required to mark vessels in one representative slice with a couple of seed-points. These points are used to learn the intensity distributions of vessels and the background, respectively. Second, a tracking approach has been proposed for segmenting (small) liver arteries [15]. To this end, a vessel template is matched to the local image data and its response is utilized in a vessel tracking scheme.

We propose a novel two-stage approach to hepatic vessel segmentation consisting in a globally optimal graph-based segmentation of larger vessels followed by robust local vessel tracking starting from the terminal centerline points of the first stage's result. In particular, our algorithm is fully automatic and adaptive to changes in contrast using a statistical parameter estimation.

2. METHODS

Given a venous-phase contrast enhanced CT scan of the liver, we first assume that a reasonably accurate segmentation of the liver is available. Such liver segmentations can be obtained fully automatically using, e.g., the approach in [16]. Additionally, to reduce noise present in the volume and to reduce inhomogenities within the liver tissue we apply Mean-Gaussian smoothing [17] as pre-processing. This curvature dependent smoothing works in a similar fashion as anisotropic diffusion without blurring across edges, while it is driven by the local geometry rather than the local constrast. Liver examples are shown with and without smoothing as maximum intensity projections (MIP) in Figure 3.

Our method consists of two principal stages. First, we focus on the detection and delineation of larger vessels, which can be characterized by a considerably good contrast to surrounding liver-parenchym compared to smaller vessels that are stronger afflicted by partial volume effects and hence exhibit less contrast to non-vessel structures. Second, starting from the segmented vessel end-points, smaller vessels are captured using a robust vessel tracking approach. In that way larger vessels are detected globally and image specific parameters (intensity contrast, noise level, ...) are estimated, while the computationally more demanding tracking algorithm is only applied in those areas where the contrast is not sufficiently high for a reliable global segmentation. Note that this tracking technique can be also applied in a semi-automatical way guided by user interaction. Each individual step is described in the following in more detail.

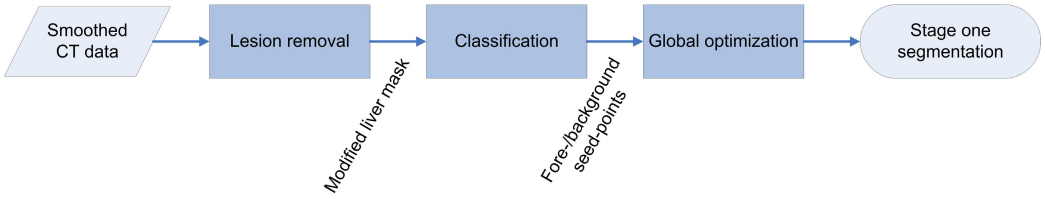

Figure 1. The global segmentation pipeline (stage 1). Regions that do not belong to the liver parenchyma or vessels are first removed resulting in a two class separation problem. Subsequently a hierarchical classifier (Figure 2) is utilized to detect foreground and background seed-points that are used as input to the graph-cuts algorithm.

2.1 Global segmentation

In the first stage we seek to obtain a reliable segmentation of the major vascular tree, while small branches might be added in a later step. The segmentation shall be especially robust against variations in contrast and signal to noise ratio caused by, *e.g.*, variations in the bolus phase, the used contrast agent, and scanner protocol, and against all kinds of liver lesions that typically occur in clinical routine.

The processing pipeline of this stage is shown in Figure 1. To acquire a robust estimation of vessel and background properties, we first segment and remove pathological regions from the liver mask. In particular, we approximately segment larger lesions and remove areas with intense Lipiodol* uptake. The original vessel segmentation objective becomes then a two class separation problem, *i.e.*, the remainder of the liver can be classified as belonging to either the vascular tree or normal liver tissue (note that since the initial lesion segmentation is not perfectly accurate, the liver tissue class might contain also other non-vessel regions in whose separation we are not further interested in). Based on three image-driven features, we compute foreground and background seed-points using an efficient hierarchical classifier (see Fig. 2) as an initial segmentation. Finally, we use the global optimal graph-cuts algorithm [18] to extract the exact vessel boundaries given the initialization.

2.1.1 Liver lesion removal

First, we detect and remove regions with intense Lipiodol uptake. Such regions which appear much brighter than vessels, can be easily detected using an upper threshold of $t_{Lipiodol} = 350$HU. All voxel intensities above $t_{Lipiodol}$ can safely be considered to be brighter than contrast enhanced vessels. Unfortunately, voxels in the immediate surrounding of those very bright regions appear in a similar intensity range as blood vessels. Hence, we dilate the original detected volume in 3D to remove the voxels with relatively high intensity values around the very bright voxels. Now, assuming the liver consists in one region of one type of tissue, which of course is not completely true as it consists of blood vessels (brighter than average), normal liver tissue, and other regions such as tumors (typically darker than average), we extract those regions that are not compatible to this null hypothesis [19].

Given the null hypothesis we estimate the global mean and global variance by the Maximum Likelihood estimates

$$\hat{\mu} = \frac{1}{N} \cdot \sum_{\mathbf{x} \in R} f(\mathbf{x}), \qquad \hat{\sigma}^2 = \left(\frac{1}{N} \cdot \sum_{\mathbf{x} \in R} f(\mathbf{x})^2 \right) - \hat{\mu}^2 \tag{1}$$

with $f(\mathbf{x})$ being the smoothed intensity values and R being the modified liver mask. Now, each Region R_n that is unlikely to comply to the null hypothesis is detected. In particular we compute the local average

$$\mu_{\mathbf{x},d} = \frac{1}{d^3} \cdot \sum_{\mathbf{x} \in S_d(\mathbf{x})} \frac{f(\mathbf{x}) - \hat{\mu}}{\hat{\sigma}^2} \tag{2}$$

in a window $S_d(\mathbf{x})$ around each $\mathbf{x}$. Assuming that no inhomogenity is present within $S_d(\mathbf{x})$, $\mu_{\mathbf{x},d}$ stems from a zero mean Gaussian distribution with variance d^{-3}. Consequently, voxels with a local average greater or smaller than a certain threshold $\pm t$ are significantly brighter or darker at a significance level s.

*Lipiodol is an iodized agent used, *e.g.*, in chemoembolization applications. It selectively remains in tumors for prolonged periods of time.

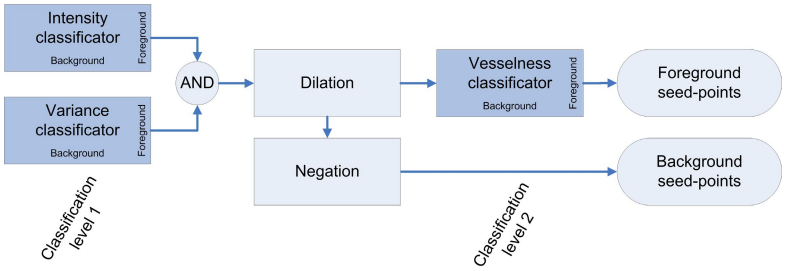

Figure 2. The hierarchical classifier used in stage 1. Foreground and background voxels are detected with a high specificity based on three image driven features, namely intensity, variance, and a vesselness feature. Note that the computationally more expensive vesselness feature is only calculated for voxels potentially belonging to the vasculature based on the first two features. The output is then used as seed-points for the graph-cuts algorithm (Section 2.1.3)

To remove lesions, significantly darker regions are marked as foreground, while the remainder (normal tissue and vessels) is marked as background. Subsequently, a smooth segmentation is obtained using the global optimal graph-cuts algorithm [18], which is also further detailed in section 2.1.3. The final output is then substracted from the liver mask.

2.1.2 Initialization

The initial segmentation is based on a hierarchical classifier that divides the voxels present in the modified liver mask into one of three classes: vessel, background, or undefined. While the first two classes are then used as seed points for the global optimization step (see Section 2.1.3), the last class basically represents the space in which the optimal vessel surfaces are efficiently found.

The hierarchical classifier consists of three basic classifiers organized in two levels (see Figure 2), while each basic classifier is implemented using the statistical threshold method already described in Section 2.1.1. The features used on the first level are the local intensity and the local variance. The parameters of these "weak" classifiers, the significance levels s_I, s_{σ^2} and the window sizes d_I, d_{σ^2} are chosen in that way that vessels are detected with a very high sensitivity. That is, voxels marked as background most certainly really belong to the background. Both foreground outputs are combined using a logical AND operator and are subsequently dilated by a small safety margin. Everything remaining is then finally marked as background for the global optimization step.

Based on the reduced subset of voxels belonging potentially to the vascular tree, we calculate a computationally more demanding local vesselness feature. For this vesselness feature we follow the idea of flux maximizing flows [20]. Imagine an elongated vessel structure that appears brighter than its surroundings, while it may have low contrast. In this case not only the magnitude, but also the direction of the gradient vector field $\mathbf{V}$ shall be considered in the vesselness measure. In particular, given a surface that is well aligned with the real vessel boundaries, the inward flux is maximized. In other words, our third feature corresponds to the divergence of the gradient vector field

$$div(\mathbf{V}) = \nabla \cdot \nabla I = \Delta I \tag{3}$$

Utilizing the divergence theorem

$$\int\int\int_{A} \Delta I \; dx \, dy \, dz = \oint_{S} \langle \mathbf{V}, \mathbf{N} \rangle \; ds \tag{4}$$

we can compute the flux feature in practice by integrating over the gradient vector field along the surface S of a sphere around a particular point $\mathbf{x}$ with $\mathbf{N}$ being the outward normal at each point of the surface. This measure allows the incorporation of a local scale by varying the radius of the sphere. A multi-scale feature is obtained by combining the flux feature at different scales r_n into a final value. To this end, we discretize the right-hand side of (4) and divide the flux by the number of entries in the discrete sum and subsequently select the flux value with the largest magnitude. It is noteworthy that the vesselness feature can be efficiently computed in parallel using multi-threading techniques or utilizing the GPU. Exemplary results are shown in Figure 3c.

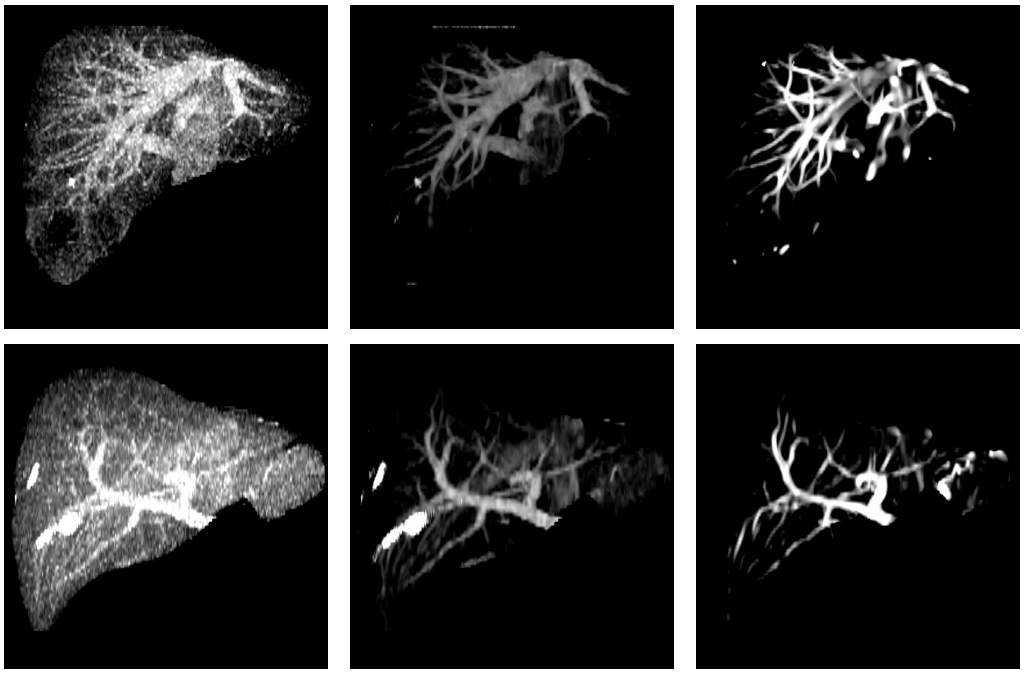

(a) (b) (c)

Figure 3. The figure illustrates exemplarily the result of the Mean-Gaussian smoothing and vessel enhancement filtering technique. (a) shows the original volume as maximum intensity projection, (b) the smoothed version, and (c) the output of the vesselness filter. Note that the filter response is only calculated for voxels potentially belonging to the vasculature after classification level one.

Based on this vesselness feature, an initial vessel segmentation with a high specificity is extracted by chosing appropriate parameters s_{flux}, d_{flux}. The so detected vessel voxels are marked as foreground for the global optimization step.

2.1.3 Global optimization

Finally, we use the global optimal graph-cuts algorithm [18] to extract the exact vessel boundaries given the detected fore- and background seed-points and the vesselness filter output. Let $G = (N, E)$ be a graph with a set of nodes N and edges E for which the graph *topology* is still to be defined. There are two types of edges, *t-links* that connect a node with the sink or source and *n-links* that connect two nodes. Each edge is weighted based on a *weighting function* to be defined. Then, graph-cuts generally minimizes a global energy function

$$E(f) = \sum_{p \in N} D_p(L_p) + \sum_{(p,q) \in E} V_{pq}(L_p, L_q) \tag{5}$$

with $D_p(l)$ being a data penalty that pixel p incurs when assigning label $l \in L = \{L_p = \{0, 1\} \,|p \in N\}$ (data term) and V_{pq} being a pairwise interaction potential that penalizes neighboring voxels that belong to different labels $L_p \neq L_q$ (smoothness term).

In our particular case, we have chosen to connect the foreground and background seed-points via infinity cost links to source and sink (data term), while the remaining nodes are only connected via n-links. In alignment with the observations in [21] we have observed that a 26 nearest neighborhood and a reciprocal weighting function

$$w_{ij} = \frac{1}{dist(v_i, v_j)} \cdot \frac{1}{1 + \beta(g(v_i) - g(v_j))^2} \tag{6}$$

performs best. Additionally a small additive constant ($1e^{-6}$) was added to each weight.

Although graph-cuts typically does not perform very well in segmenting elongated shapes because it often tends to be biased towards shorter boundaries, it is still very well suited for vessel segmentation in our case. Specifically note that the foreground seed-points are concentrated in the vessel center as the vesselness filter output is maximal in that area while it might be lacking in some areas such as bifurcations. Given these vessel regions, which might be disconnected, graph-cuts is capable of delineating the vessel surface accurately and merging disconnected branches.

To this end, we apply the graph-cuts method consecutively with two different parameter settings. One can observe that given the previously described initialization a large beta factor (*i.e.*, small smoothness term) is advantageous for connecting disconnected pieces, while a small beta factor (*i.e.*, large smoothness term) provides a more accurate delineation of the vessel boundaries. Consequently we solve the graph cuts equation first with $\beta_1 = 10$ and use the updated foreground mask as initialization for a second graph cuts method with $\beta_2 = 0.0001$. The outcome is then the final vessel segmentation. In a postprocessing step, we remove regions with less than N_{cc} voxels, based on a connected-component analysis.

2.2 Local tracking

In the second stage we extend the segmented vessel trees including also smaller vessels. To this end, we extract the centerline structure of the already segmented vessels [22] and detect automatically all terminal points. Starting from these sites, we apply a robust tracking approach similar to the one we have recently proposed for general vessel tree modelling [23].

2.2.1 Centerline extraction

The centerline extraction method [22] requires a preselected root site along the binary segmentation as input. To this end, for each connected component remaining in the binary segmentation mask after the postprocessing step, a root site is automatically selected by determining the point with maximal distance to all segmented surfaces. Then, the 3D skeleton of the segmented vascular structure is computed and stored in a tree data structure T. Based on T, several post-processing steps that might delete or move centerline points as well as delete false branches, are applied. In particular, branches that are created because of small irregularities on the vessel surface and those shorter than twice the radius at the bifurcation point get eliminated. Finally, intermediate sites are eliminated and smooth branches are created using a spline fitting. As an output we also get a list of all terminal sites, which are used as seed-points for the subsequent local vessel tracking.

2.2.2 Centerline tracking algorithm

The centerlines of remaining unsegmented vascular structures are extracted via a graph-based tracking algorithm using multi-scale medialness-filters. Specifically, the algorithm has four componenents: First, a *medialness* measure based on 2D multi-scale cross-sectional models is introduced. This new measure is contrast and scale independent and it works well in the presence of nearby bright structures such as other vessels. Second, a minimal path detection method working on a discrete grid where the cost of the graph edges are computed from this medialness filter. Third, the full vessel centerline tree is extracted from a single seed-point by a post-processing algorithm, which uses the length and scale of the vessel centerlines. In general, the proposed method can extract the centerline for a vessel segment as well as for a full vessel tree. Fourth, the exact vessel boundaries are delineated from its centerline structure.

Medialness measure from 2D cross-sectional models First, we introduce a medialness measure that is based on multi-scale cross-sectional vessel modeling. Blood vessels in CTA typically have circular/elliptic shapes in cross-sectional views even though local variations on them are not too uncommon due to the presence of nearby vessels or pathologies. Ideally, 2D cross-sectional vessel profiles consist of a circular/elliptic bright disk and a darker ring around them (Figure 4a). Our medialness measure uses this circularity assumption and expected intensity profile. To this end, we cast a number of rays from the center point and collect intensity profiles along them. The typical intensity profile of a vessel and its immediate background starting from the center is shown in Figure 4b. This 1D vessel intensity model is further divided into three intervals, R_I, R_O, R_B (Figure 4c). Specifically, the region inside a vessel along a ray, R_I can be represented by a bright and roughly flat intensity profile whose size depends on the radius of the vessel. Similarly, the region outside a vessel along a ray R_O

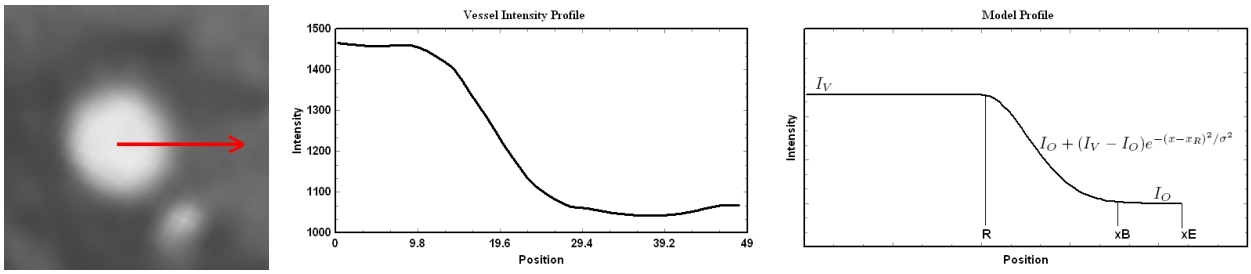

(a) (b) (c)

Figure 4. This figure shows a typical vessel in cross-sectional view (a) and the intensity profile along a 1D ray starting from the center (b). In our vesselness filter design, we model this intensity profile by dividing it into three intervals, inside, outside, and boundary.

can be represented by a darker and roughly flat intensity profile whose size depends on the presence of nearby structures. The boundary region between vessel and background, R_B, can be described by a Gaussian profile. Mathematically, the vessel intensity model along a ray equals

$$V(x,R,\sigma) = \begin{cases} I_V & \text{if } x \geq 0 \text{ and } x < R \\ I_O + (I_V - I_O)e^{-(x-R)^2/\sigma^2} & \text{if } x \geq R \text{ and } x < x_B \\ I_O & \text{if } x \geq x_B \text{ and } x < x_E \end{cases} \tag{7}$$

where R is the radius and I_V and I_O are the average intensity values inside and just outside a vessel, respectively. In addition, we set $x_B = R + 2\sigma$ and $x_E = x_B + 1$ in our experiments. An intensity profile, I, obtained from the original CTA/MRA data along a ray should match the profile of the proposed 1-D intensity vessel model, V, if the observed data I is sampled from a vessel. Specifically, we use the difference between the measured intensity profile I and the vessel model V as a fit measure in our vesselness criteria. That is, the fit measure f_i along a ray, is given by $f_i = min_{R,\sigma}||V_i(R,\sigma) - I_i||^2$. Then, the medialness measure $VM(x,y,z)$ of a point is given from the summation of such fit measures along all rays, *i.e.*, $VM(x,y,z) = \sum_{i=1}^{N} f_i$ where N is the total number of rays. Observe that our vessel intensity model contains two important values, namely, I_V and I_O. Their value plays a very strong role in the accuracy of the matched filter. In our implementation, the results of the global optimization stage (Section 2.1.3) allows us to estimate these values accurately.

Center-axis extraction from graph-based optimization In this section, we first summarize a method for extracting the local center axis between a source and a sink by integrating the medialness map in a discrete optimization framework and then show how to extract the full vessel centerline tree from a single seed-point. Specifically, we seek to obtain a curve $C(s)$ (center axis) between points p_0 and p_1 which travels through the center of a vessel. This problem can be successfully solved by the *minimum-cost* path detection algorithms [24,25]: Let $E(C)$ be the total energy along a curve C

$$E(C) = \int_{\Omega} (P(C(s)) + w)\, ds \tag{8}$$

where $P(C)$ is called potential, w is the regularization term and s is the arch length, *i.e.*, $||C(s)||^2 = 1$. In vessel centerline extraction methods, the potential $P(x)$ at x corresponds to the inverse of a medialness measure at that location, namely, $P(x) = \frac{1}{m(x)}$. Let A_{p_0,p_1} represent the set of all curves between p_0 and p_1. The curve with total minimal energy can be computed from the *minimum-accumulative cost*, $\phi(p)$, which measures the minimal energy at p integrated along a curve starting from the point p_0:

$$\phi(p) = \inf_{A_{p0,p1}} \{E(C)\} \tag{9}$$

In this paper, we use Dijkstra's algorithm for solving equation (9) in a discrete domain. Specifically, let $G = (N,E)$ be a discrete graph where N and E represent nodes and edges, respectively. The minimum-accumulative

cost at the node P_{ij} for a four connected 2D graph is then given by

$$\phi(P_{ij}) = \min\left(\phi(P_{i-1j}) + C^{ij}_{(i-1)j}, \phi(P_{i+1j}) + C^{ij}_{(i+1)j}, \phi(P_{ij-1}) + C^{ij}_{i(j-1)}, \phi(P_{ij+1}) + C^{ij}_{i(j+1)}\right) \tag{10}$$

where, for example, $C^{ij}_{(i-1)j}$ corresponds to the cost of propagation from point $P_{(i-1)j}$ to P_{ij} which is obtained from the inverse of the medialness measure. This algorithm can be easily implemented by first setting the minimum-accumulative cost of all nodes to infinity (or a large value) and then using an explicit discrete front propagation method where propagation always takes place from the minimum value to its neighboring nodes. In our implementation, we use a 27-connected lattice in 3D, *i.e.*, diagonal propagations are also included for better accuracy. In addition, the medialness measure is computed orthogonal to the direction of the propagation instead of computing it at the nodes. The discrete path (curve) from a point P_{ij} to source P_0 can then be easily obtained by traversing (backtracking) along the propagation.

This centerline extraction algorithm starts from a source and it terminates when the front propagation reaches to a *sink*, *i.e.*, an end point. When there is no sink point defined for an explicit stopping, the propagation should continue until it reaches the end of all branches, *i.e.*, a stopping criteria is met. Specifically, in our task, the propagation starts from all seed-points that are determined in Section 2.2.1. The stopping criteria is based on the medialness measure along a discrete front. Specifically, propagation is forced to stop when the minimum medialness measure along a discrete front at any time drops below a threshold.

While this iterative minimization algorithm constructs the accumulative cost map, ϕ, it does not explicitly detect the centerline structure of a vascular tree since there are no user placed end points. Observe that it is possible to detect the minimum-cost path between front pixels and the source. Most of these paths correspond to the discontinuities of the propagating fronts. We propose that the determination of correct paths depends on their *saliency*. The saliency of a branch is determined from its length and the size of the maximum medialness filter along that branch. Specifically, we first start a path detection process from a front point that has the maximum distance from the source, which results in a discrete centerline. This path detection process is iteratively applied to each front point by always selecting the one with the maximum distance to the existing centerline. This algorithm then detects all salient vessel centerlines starting from a single source. The same algorithm is applied to all the fronts starting from the different seed-points that correspond to the terminal points of the previous detected vascular tree.

Vessel mask delineation from centerline structure Given the newly detected centerline structures for which an approximate vessel radius is also available as another output from the multi-scale medialness filter, we finally seek to create the corresponding binary masks. To this end, we utilize again the already earlier described graph-cuts algorithm. We convert the new centerline points and its immediate surroundings up to a minimal radius to foreground seed-points. This minimal radius corresponds to the minimal radius of interest for the application and equals also to the minimal radius used for the multi-scale matched filter. Image points further away than a maximal radius to the centerline, while this radius corresponds to a slightly increased version of the maximal radius of the branch as detected by the used filter, are marked as background. Then, graph-cuts (see Section 2.1.3) is applied to delineate the optimal surface.

2.3 User-guided tracking

In a clinical environment, it is important to provide tools to modify and correct the automatic segmentation result to the user. In particular it should be possible to add missed branches or subtrees with minimal user interaction. The tracking algorithm as described in Section 2.2.2 can be also utilized for this purpose. An example is shown in Figure 5. Given the results from the fully automatic algorithm, the tracking algorithm is started again from an interactively selected seed-point. The newly detected centerline is then connected to the centerline corresponding to the original vessel mask voxel that is visited first during the propagation process. Note that the propagation is performed in every direction starting from the seed-point so that this point is not only connected to the existing segmentation, but vessel parts beyond the seed-point are also explored. While the portion of the newly detected centerline structure between the seed-point and the existing segmentation is kept in every case as we assume that the marked voxel really belongs to the vascular tree, the portion distal to the seed-point is further validated to avoid leakage. In particular centerline pieces for which its cumulative

medialness response does not exhibit a certain minimal value, get erased. The corresponding binary mask is then finally computed using again the graph-cuts algorithm as described earlier. Note that the visualized centerline structure corresponds to the newly added branches only.

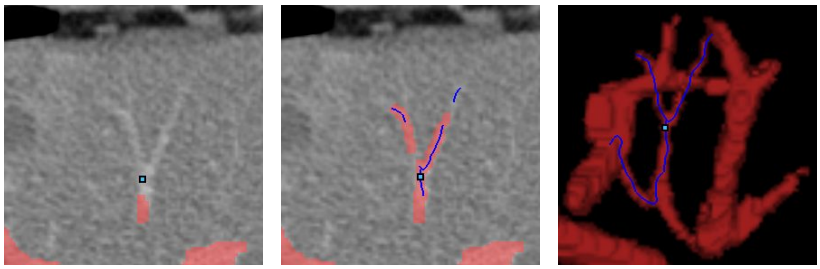

(a) (b) (c)

Figure 5. Example that shows the user-guided tracking. In (a) a missing sub-tree is marked by one seed-point. The tracking result (blue centerlines) and the corresponding segmentation mask are shown in (b) and (c), respectively.

3. RESULTS

The proposed system has been evaluated on 30 venous phase liver CT scans from clinical routine and demonstrates overall promising results. The resolution of those data sets ranged from $0.53 - 0.88$ mm/Voxel in the axial plane (average of 0.71 mm) and $0.6 - 3.0$ mm/Voxel in z-direction (typically either 1.0, 1.5, or 2.0 mm). The number of slices varies from 66 to 505. The data was acquired at different clinical sites exhibiting a wide range on image quality and liver pathologies. In particular some of the livers contain extremely large and/or multiple lesions.

All livers have been fully automatically detected and segmented using the method in [16] without any further postprocessing. In the rare case that the liver segmentation has leaked into the kidney (2 out of 30 cases), the kidney part has been spuriously also segmented as vessels because of its bright intensity values. This could have been easily avoided by improving the liver segmentation or interactively editing of the liver mask.

For the tumor segmentation we have chosen a window size of $d = 5$ voxel and a significance level $s = 6e^{-5}$. All parameters have been chosen empirically. For the consecutively applied graph-cuts algorithm we have chosen the reciprocal weighting function (6) with $\beta = 150$. Exemplary results are shown in Figure 6. Note that tumor segmentation is not the main objective and that the proposed method is not capable in segmenting very small lesions or lesions with similar intensity characteristics as the parenchyma.

The hierarchical classifier has been applied with a parameter setting of $d_I = 3$ voxel, $s_I = 6e^{-5}$ for the intensity feature, $d_{\sigma^2} = 5$ voxel, $s_{\sigma^2} = 2e^{-3}$ for the variance feature, and $d_{flux} = 3$ voxel, $s_{flux} = 3e^{-1}$ for the vesselness feature. The vesselness measure has been calculated for radii $r = \{2, 3, 4, 5\}$ mm. Finally, components with less than $N_{cc} = 250$ voxel have been disregarded. Figure 7 exemplifies the two-stage concept. Subfigure (a) shows two results of the global segmentation, which has detected the main branches with a high specificity.

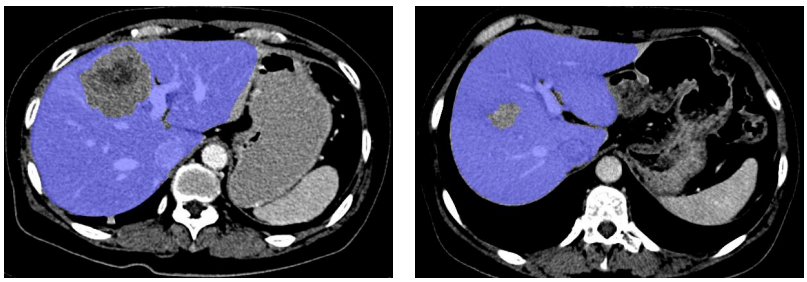

Figure 6. The figure shows two results of the tumor segmentation method. The modified liver mask is shown as blue overlay.

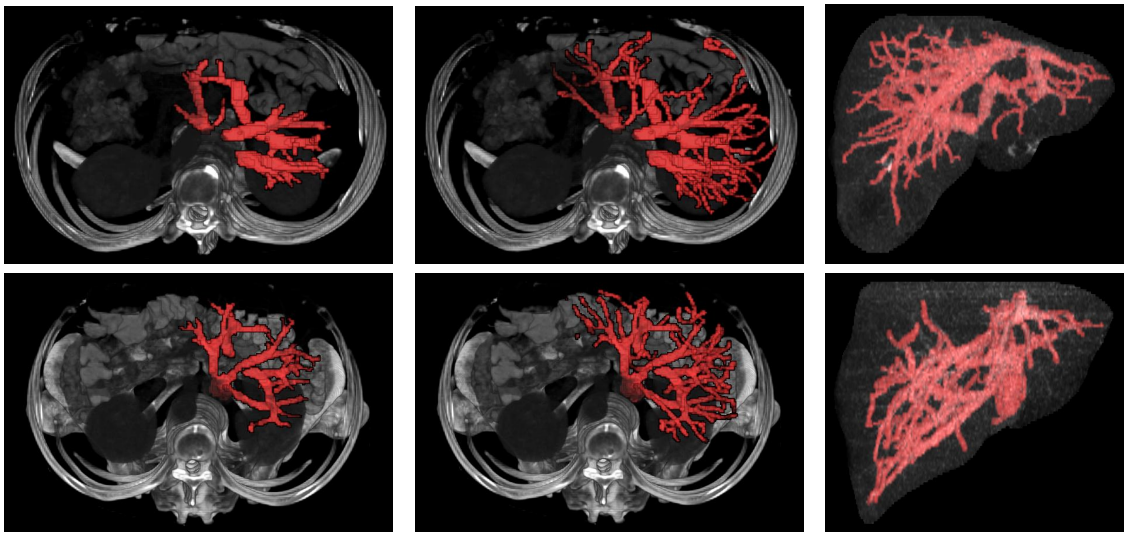

(a) (b) (c)

Figure 7. This figure shows the segmentation result of the larger vessels (a) and the results including the vessel tracking step (b) in head view. In (c) the final result is shown in red within the MIP anterior view of the segmented liver.

Note that these figures have been created with a slightly different parameter setting so that both stages can be more distinctively recognized. Generally speaking, higher significance levels during the global segmentation step will create a segmentation with a higher specificity but lower sensitivity, while lower levels will result in a more complete segmentation which might also contain false positives. The above listed parameters have so far proven being the best trade-off based on visual inspection. The centerline end-points have then been used for the computational more demanding vessel tracking step. Results including large and small vessels are finally shown in Figure 7b,c in head view and within the MIP anterior view of the segmented liver, respectively. Depending on the application, the global segmentation results might already be sufficient.

Further results are shown in Figure 8. The first column shows for each case the extracted centerline structure as overlay on a MIP of the liver. The second column is then the corresponding binary mask of the segmented vessels. The following three columns show randomly selected axial slices with a LUT setting of center/width = 90/190 HU, while the segmentation results are shown as red overlays. The liver segmentation is visible as thin green contour that contains the segmented liver.

Beside the fully automatic instance of the proposed system, the vessel tracking approach allows to conveniently add missing branches/sub-trees by simply adding a single seed-point into the branch of interest. An example is shown in Figure 5.

4. CONCLUSIONS

We have presented a fully automatic approach to segment the hepatic vascular tree in CT images. The system combines a globally optimal graph-cut-based segmentation with robust local vessel tracking. The approach is robust to variations in intensities of vessels and their surroundings which may contain tumors. In addition, different sized vessels (large and small) are obtained accurately by the use of the proposed two-stage segmentation algorithm without excessive computational requirements. Furthermore, the vessel tracking approach can be utilized to add interactively missing branches or sub-trees by simply adding single seed-points. For the future we especially plan to further validate the proposed system based on a semi-automatically created ground truth and to learn the involved parameters from this reference.

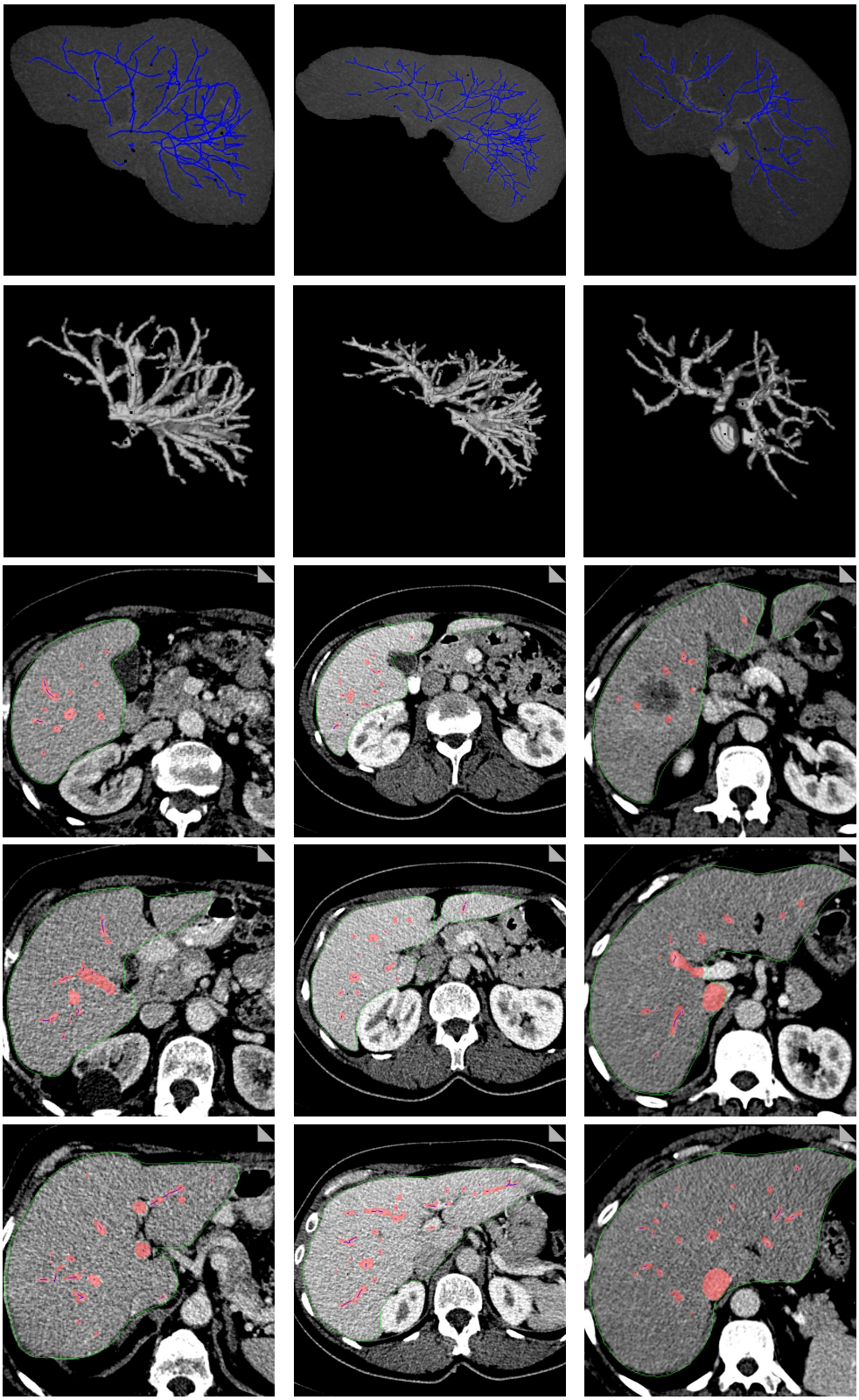

Figure 8. This figure shows in column one the extracted centerline on top of the MIP and in colum two a 3D rendering of the segmented tree. The remaining columns show the segmentation result as overlay to randomly selected 2D slices.

REFERENCES

1. E. K. Fishman, B. S. Kuszyk, D. G. Heath, et al., "Surgical Planning for Liver Resection," *Computer* **29**(1), pp. 64–72, 1996.
2. G. Low, E. Wiebe, A. Walji, and D. Bigam, "Imaging evaluation of potential donors in living-donor liver transplantation," *Clinical Radiology* **63**(2), pp. 136–145, 2008.
3. M. J. Bassignani, A. S. Fulcher, R. A. Szucs, et al., "Use of Imaging for Living Donor Liver Transplantation," *Radiographics* **21**(1), pp. 39–52, 2001.
4. C. Couinaud, *Le Foie - Etudes anatomiques et chirurgicales*, Masson, Paris, 1957.
5. D. Selle, B. Preim, A. Schenk, and H. O. Peitgen, "Analysis of Vasculature for Liver Surgical Planning," *IEEE Trans Med Imaging* **21**(11), pp. 1344–1357, 2002.
6. M. Erdt, M. Raspe, and M. Sühling, "Automatic Hepatic Vessel Segmentation using Graphics Hardware," in *4th Int Workshop on Medical Imaging and Augmented Reality (MIAR)*, *LNCS* **5128**, pp. 403–412, 2008.
7. R. Beichel, T. Pock, C. Janko, and et al., "Liver Segment Approximation in CT Data for Surgical Resection Planning," in *SPIE Medical Imaging*, **5370**, pp. 1435–1446, 2004.
8. P. Makowski and S. Casciaro, "Review of Vessel Segmentation Methods Applied to Liver Volume Images," in *Minimally Invasive Technologies and Nanosystems for Diagnosis and Therapies*, S. Casciaro and E. Samset, eds., pp. 103–112, Lupiensis Biomedical Publications, 2008.
9. L. Soler, H. Delingette, G. Malandain, et al., "Fully automatic anatomical, pathological, and functional segmentation from CT scans for hepatic surgery," in *SPIE Medical Imaging*, **3979**, pp. 246–255, 2000.
10. L. Soler, H. Delingette, G. Malandain, et al., "Fully automatic anatomical, pathological, and functional segmentation from CT scans for hepatic surgery," *Computer Aided Surgery* **6**(3), pp. 131–142, 2001.
11. D. Selle, *Analyse von Gefäßstrukturen in medizinischen Schichtdatensätzen für die computergestützte Operationsplanung*. PhD thesis, Universität Bremen, 1999.
12. D. Selle, W. Spindler, B. Preim, and H.-O. Peitgen, "Mathematical Methods in Medical Imaging: Analysis of Vascular Structures for Liver Surgery Planning," in *Mathematics Unlimited - 2001 and Beyond*, B. Enquist and W. Schmid, eds., pp. 103–109, Springer, 2001.
13. Y. Sato, S. Nakajima, N. Shiraga, et al., "Three-dimensional multi-scale line filter for segmentation and visualization of curvilinear structures in medical images," *Medical Image Analysis* **2**(2), pp. 143–168, 1998.
14. H. Homann, G. Vesom, and J. A. Noble, "Vasculature segmentation of CT liver images using graph cuts and graph-based analysis," in *5th IEEE Int Symposium on Biomedical Imaging, ISBI*, pp. 53–56, 2008.
15. O. Friman, M. Hindennach, and H.-O. Peitgen, "Template-based multiple hypotheses tracking of small vessels," in *5th IEEE Int Symposium on Biomedical Imaging, ISBI*, pp. 1047–1050, 2008.
16. H. Ling, S. Zhou, Y. Zheng, et al., "Hierarchical, Learning-based Automatic Liver Segmentation," *IEEE Conf on Computer Vision and Pattern Recognition, CVPR* , pp. 1–8, 2008.
17. P. Neskovic and B. B. Kimia, "Geometric Smoothing of 3D Surfaces and Non-linear Diffusion of 3D Images," tech. rep., Division of Engineering, Brown University, 1995.
18. Y. Boykov and V. Kolmogorov, "An Experimental Comparison of Min-Cut/Max-Flow Algorithms for Energy Minimization in Vision," *IEEE Trans. Pattern Anal. Mach. Intell.* **26**(9), pp. 1124–1137, 2004.
19. T. Aach and H. Dawid, "Region oriented 3D-segmentation of NMR-datasets: A statistical model-based approach," in *SPIE Visual Communications and Image Processing*, **1360**, pp. 690–701, 1990.
20. A. Vasilevskiy and K. Siddiqi, "Flux Maximizing Geometric Flows," *IEEE Int Conf on Computer Vision, ICCV* **1**, pp. 149–154, 2001.
21. L. Grady and M.-P. Jolly, "Weights and Topology: A Study of the Effects of Graph Construction on 3D Image Segmentation," in *Proc. of MICCAI 2008*, *LNCS* **5241**, pp. 153–161, 2008.
22. A. P. Kiraly, J. P. Helferty, E. A. Hoffman, et al., "Three-Dimensional Path Planning for Virtual Bronchoscopy," *IEEE Trans. Med. Imaging* **23**(11), pp. 1365–1379, 2004.
23. M. A. Gülsün and H. Tek, "Robust Vessel Tree Modeling," in *Proc. of MICCAI 2008*, *LNCS* **5241**, pp. 602–611, 2008.
24. T. Deschamps and L. Cohen, "Fast extraction of minimal paths in 3D images and applications to virtual endoscopy," *Medical Image Analysis* **5**(4), pp. 281–299, 2001.
25. K. Siddiqi and A. Vasilevskiy, "3D Flux Maximizing Flows," in *Int Workshop on Energy Minimizing Methods In Computer Vision*, *LNCS* **2134**, pp. 636–650, 2001.